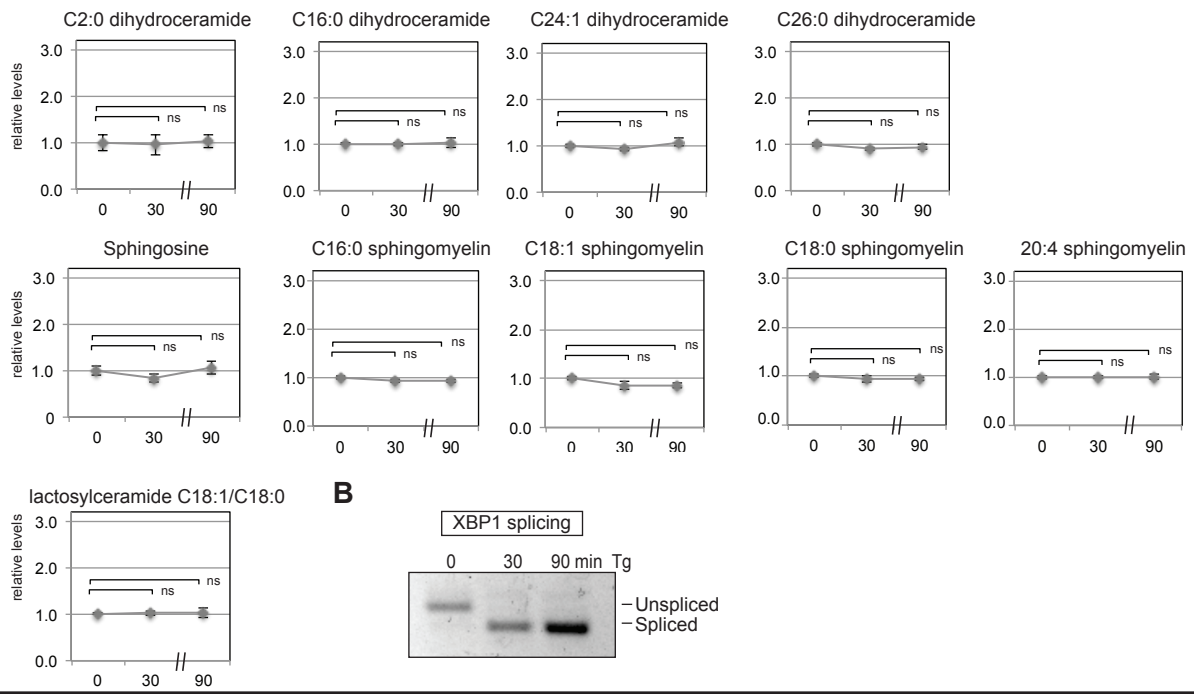
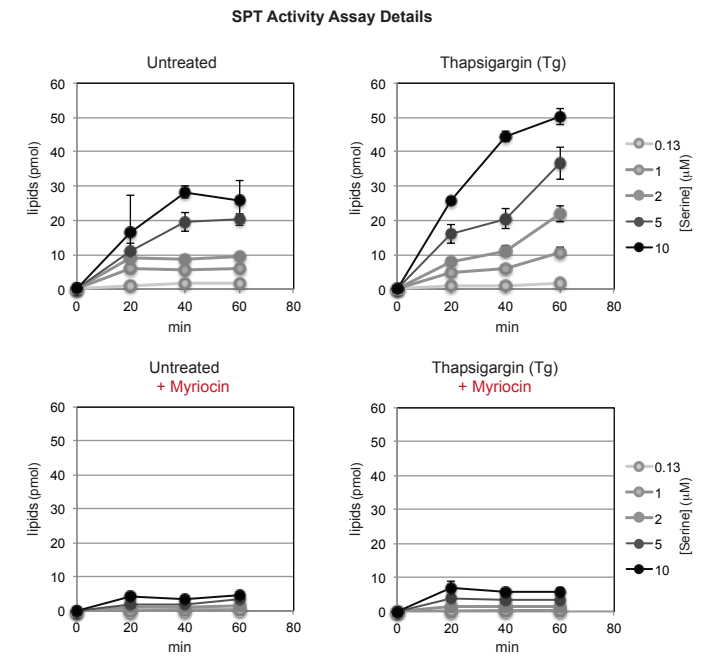


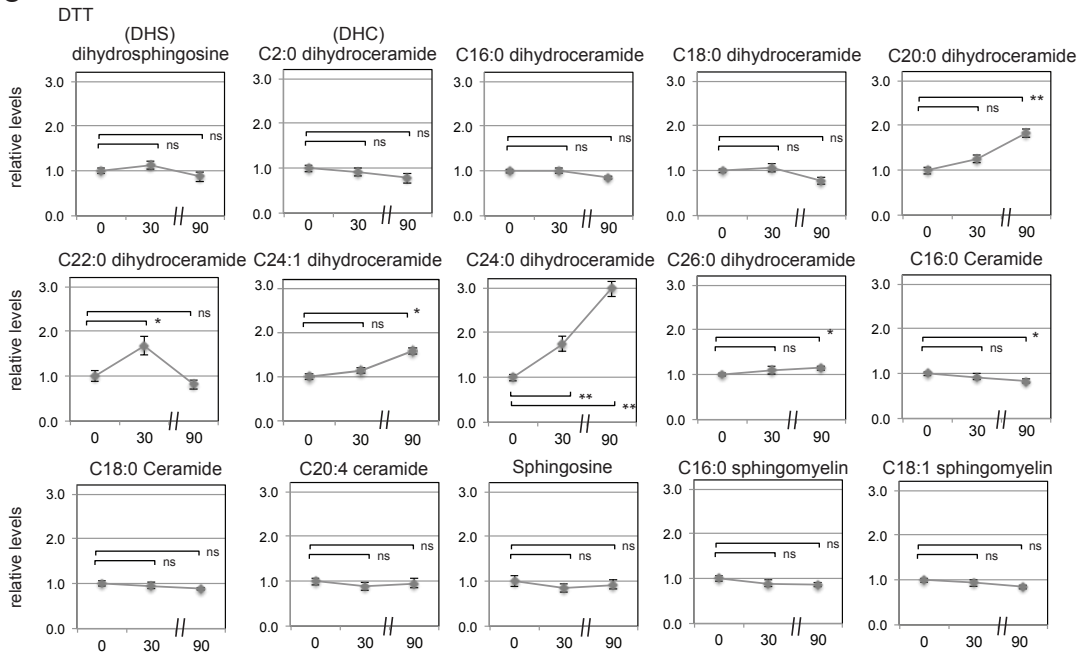
A Thapsigargin (continued from Figure 1B)



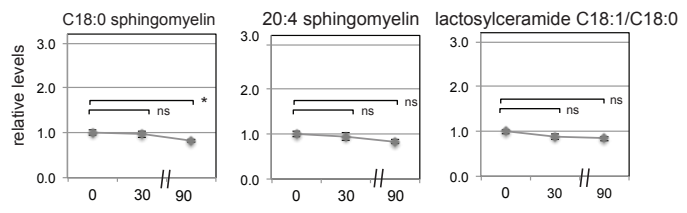
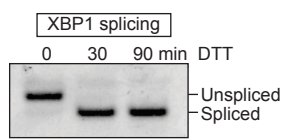
E



C



D



p value - comparing Unt vs Tg treated

Untr	0	20	40	60
0.13	ns	ns	ns	ns
1	ns	ns	ns	**
2	ns	ns	*	**
5	ns	ns	ns	**
10	ns	*	**	**

p value - comparing Unt+Myr vs Tg+Myr treated

Myr+Untr	0	20	40	60
0.13	ns	ns	ns	ns
2	ns	ns	ns	ns
5	ns	*	*	ns
10	ns	ns	ns	**

Supplemental Figure 1. Mass Spec Analysis of *de novo* Sphingolipid Levels during Thapsigargin (Tg)-induced UPR, related to Figure 1.

(A) In HEK293 cells treated with 200 nM thapsigargin (Tg) for up to 90 min, levels of C2:0, C16:0, C24:1 C26:0 dihydroceramide (DHC), sphingosine, C16:0, C18:1 C18:0, C20:4 sphingomyelin, and lactosylceramide C18:1/C18 did not change. Levels of additional lipids including DHS, C18:0, C20:0, C22:0, C24:0 DHC, C16:0 C18:0, and C20:4 ceramide, from the same mass spec experiments are shown in Figure 1B. Note that the distance between 30 and 90 min timepts is foreshortened to save space in this and panel S1C; the fold-induction over 0min is the key comparison. Data are means \pm SD of five independent mass spectrometry analyses. Statistical significance was calculated using unpaired two-tailed t-tests and ** indicates $p < 0.01$ comparing treated and untreated samples.

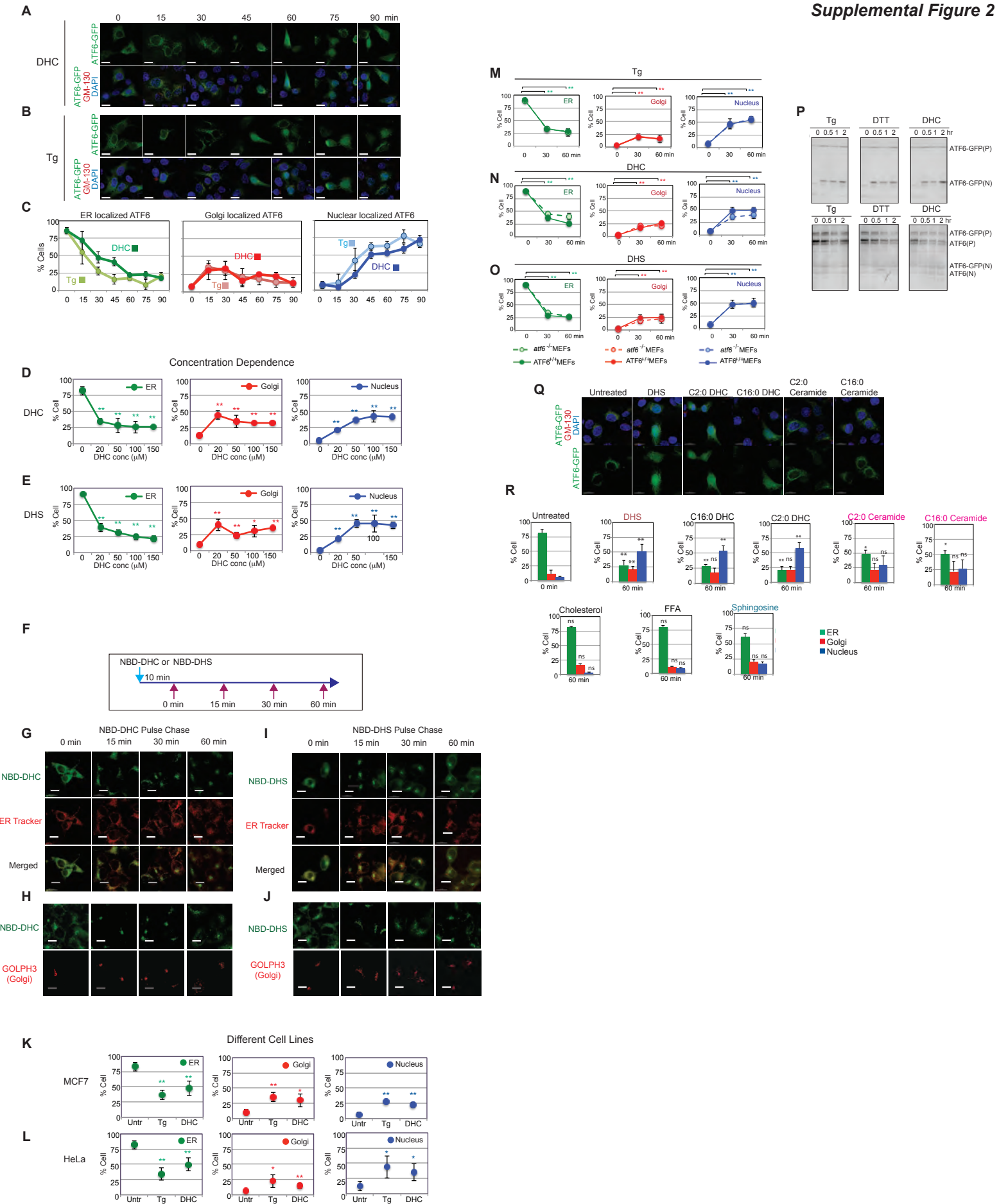
(B) *XBP1* splicing occurred effectively in cell samples used for mass spectrometry analyses. HEK293 cells were treated with Tg for indicated amounts of time and activation of the UPR was analyzed by the appearance of spliced *XBP1* mRNA. Unspliced and spliced forms of *XBP1* mRNA are indicated.

(C) The mass spectrometric analysis of sphingolipids in DTT-treated HEK293 cells showed an increase in C20:0, C22:0, C24:1, C24:0 DHC but not downstream sphingolipids. Levels of DHS, C2:0, C16:0, C18:0, C20:0, C22:0, C24:1, C24:0, and C26:0 DHC, C16:0, C18:0, and C20:4 ceramide, sphingosine, C16:0, C18:1, C18:0, and C20:4 sphingomyelin, and C18:1/C18:0 lactosylceramide in HEK293 cells treated with 1 mM DTT for up to 90 min are shown. Data are means \pm SD of five independent experiments. Statistical significance was calculated using unpaired two-tailed t-tests and ** indicates $p < 0.01$ comparing treated and untreated samples.

(D) *XBP1* splicing shows that ER stress was effectively induced during DTT treatment of HEK293 cells used for mass spec analyses. Unspliced and spliced forms of *XBP1* mRNA are indicated.

(E) Tg treatment increased levels of sphingolipid synthesis. To determine whether increased levels of DHS during ER stress (Figure 1B and Figures S1A and S1C) resulted from increased DHS synthesis, activities of enzymes involved in sphingolipid synthesis in the ER

(including serine palmitoyltransferase (SPT), 3-dehydrosphinganine reductase (FVT-1), ceramide synthase (CerS), and sphingolipid delta(4)-desaturase (DES1)) were tested in *in vitro* using microsomes generated from HEK293 cells that were treated with Tg for 90 min. Newly generated sphingolipids were measured by the incorporation of radiolabeled serine (^3H -serine), a starting component of sphingolipids. For each concentration of ^3H -Serine added, a time course was performed, measuring the amount of ^3H -labeled lipids (pmol). Comparisons were made between untreated cells (top left panel), Tg-treated cells (top right panel), 25 mM myriocin-treated cells (bottom left panel), and cells treated with Tg + 25 mM myriocin (bottom right panel). Addition of myriocin to both untreated and Tg-treated extracts dramatically reduced production of ^3H sphingolipids. More details are described in the *in vitro* SPT assay experimental procedure.



Supplemental Figure 2. Dihydrosphingosine (DHS) and Dihydroceramide (DHC) Activate ATF6, related to Figure 2.

(A–C) Detailed time course of ATF6-GFP activation in HEK293 cells treated with DHC (50 μ M) (A) or Tg (200 nM) (B). Golgi was visualized using antibodies against GM130 (red); DAPI (blue) was used to label nuclear DNA. Representative fields of cells are shown for each time point. Percentages of cells in which ATF6 localized to the ER, Golgi, and nucleus are shown in (C). Data are means \pm SD of at least three independent experiments, \geq 50 cells per time point.

(D–E) Dose-dependent effects of DHC (D) and DHS (E) on ATF6-GFP activation. ATF6-GFP localization to the ER (green), Golgi (red), and nucleus (blue) in HEK293 cells showed that ATF6 activation (the appearance of nuclear-localized ATF6) increased upon treatment with increasing concentrations of DHC (D) or DHS (E) for 60 min. ATF6 activation reached a plateau at 50 μ M of DHC or DHS. Data are means \pm SD, and each experiment was independently repeated at least three times, \geq 50 cells for each time point. Statistical significance ** $p < 0.01$, * $p < 0.05$ was calculated via unpaired two-tailed t-tests.

(F) A schematic of experiments testing the subcellular localizations of NBD-labeled DHS or DHC upon addition to HEK293 cells. NBD-DHS or -DHC was added to cells for 10 min before cells were placed in media without NBD-labeled lipids. Localizations of NBD-labeled lipids were visualized at indicated time points.

(G–J) Localizations of NBD-labeled lipids at each time point after chasing with fresh media showed that NBD-DHS (I, J) and NBD-DHC (G, H) initially localized to the ER, then moved to the Golgi. Both DHS and DHC are early intermediates of the sphingolipid biosynthetic pathway (Figure 1A) for downstream lipids synthesized at the Golgi. Co-staining with ER tracker (G, I) and anti-Golph3 (H, J) revealed the locations of the ER and Golgi.

(K–L) ATF6 localized to the ER (green), Golgi (red), and nucleus (blue) in MCF7 breast cancer cells (K) or HeLa cervical cancer cells (L) showing that DHC activated ATF6 similarly to Tg treatment, and that DHC can activate ATF6 in cell types other than

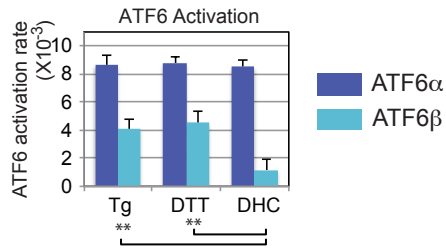
HEK293 cells. Cells were treated with 200 nM Tg or 50 μ M DHC for 60 min and then analyzed as described in Figure 2. Statistical significance ** $p < 0.01$, * $p < 0.05$ was calculated via unpaired two-tailed t-tests.

(M-O) Similar effects on ATF6-GFP localization were seen in *atf6*^{-/-} (ATF6 knock out) or ATF6^{+/+} (ATF6 wild-type) mouse embryonic fibroblasts (MEFs) treated with 200 nM Tg (M), 50 μ M DHC (N), or 50 μ M DHS (O) for 60 min. Data are means \pm SD of at least three independent experiments, ≥ 50 cells per time point.

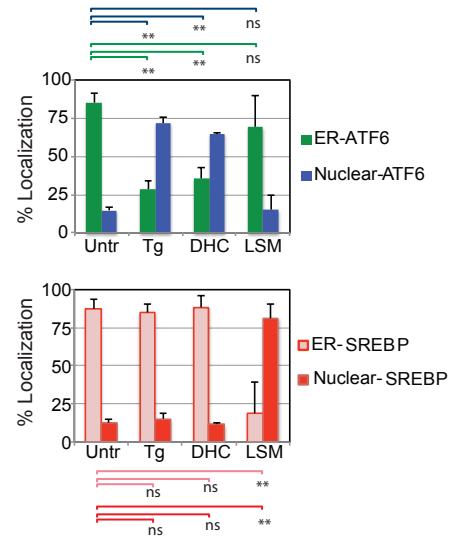
(P) ATF6-GFP was cleaved when HEK293 cells were treated with Tg (200 nM), DTT (1 mM), or DHC (50 μ M) for 2 h. Western blotting (using an anti-GFP antibody, top) showed full-length ATF6-GFP (P) and the activated nuclear form of ATF6-GFP (N). Re-probing the same blot with anti-ATF6 antibody (bottom) showed the endogenous full-length ATF6 (P) and the nuclear form of ATF6 (N).

(Q-R) Activation of ATF6 by DHC and DHS is specific, and is not seen at significant levels when other lipids are added (e.g., ceramide, sphingosine, palmitic acid (FFA), or cholesterol). Representative fields of ATF6-GFP in untreated HEK293 cells, or cells treated with DHS, C2:0 DHC, C16:0 DHC, C2:0 ceramide, or C16:0 ceramide. Golgi localization was visualized using an antibody against the Golgi-localized protein, GM130. Note that C2:0 and C16:0 DHC both effectively activate ATF6. Data are means \pm SD and each experiment was independently repeated at least three times, ≥ 50 cells for each time point. Statistical significance ** $p < 0.01$, * $p < 0.05$ was calculated via unpaired two-tailed t-tests comparing untreated and treated samples.

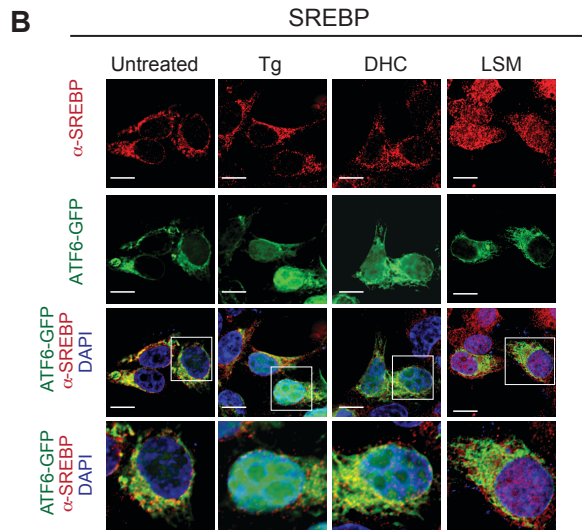
A



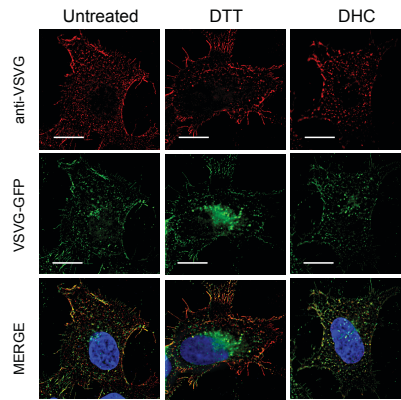
C



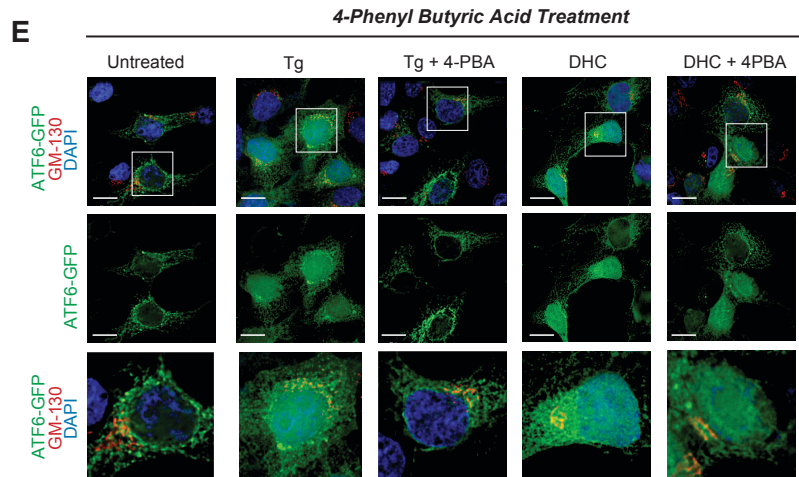
B



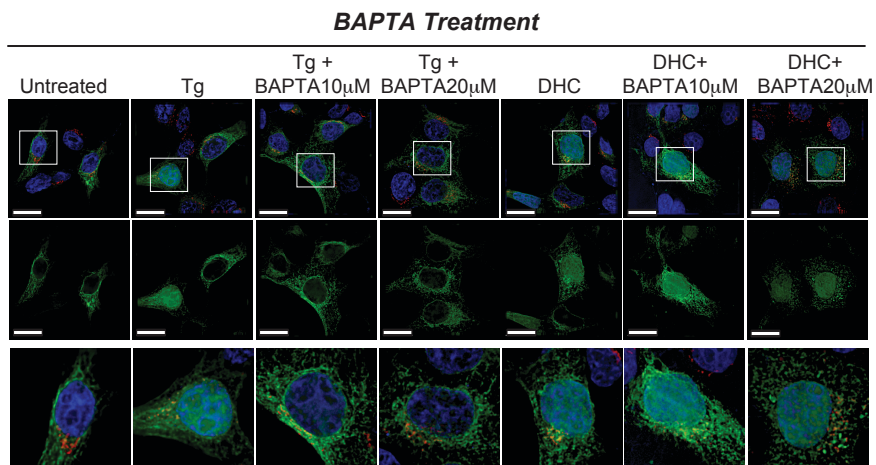
D



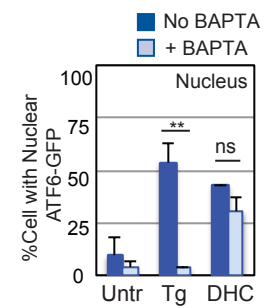
E



F



G



Supplemental Figure 3. Mechanism by which DHC Activates ATF6, related to Figure 3.

(A) Little activation of ATF6 β by DHC. Activation rate of ATF6 β (light blue) in HEK293 cells treated with Tg (200 nM), DTT (1 mM), or DHC (50 μ M) for 1 h shows that ATF6 β is not activated by DHC. For comparisons, ATF6 α activation rates (dark blue) upon treatment with Tg (200 nM), DTT (1 mM), or DHC (50 μ M) for 1 h are shown. Data are means \pm SD and each experiment was independently repeated at least three times, \geq 50 cells for each time point. Statistical significance ** $p < 0.01$, * $p < 0.05$ was calculated via unpaired two-tailed t-tests comparing DHC treated with Tg or DTT treated samples.

(B-C) SREBP is not activated by DHC or Tg. SREBP is another ER transmembrane transcription factor, like ATF6. However, SREBP (red) was activated, i.e., was cleaved and entered the nucleus, when HEK293 cells were incubated in low serum media (LSM), but not with Tg or DHC. Localization of SREBP was monitored using antibodies against SREBP. Data are means \pm SD and each experiment was independently repeated at least three times, \geq 50 cells for each time point. Statistical significance ** $p < 0.01$, * $p < 0.05$ was calculated via unpaired two-tailed t-tests comparing untreated and treated samples.

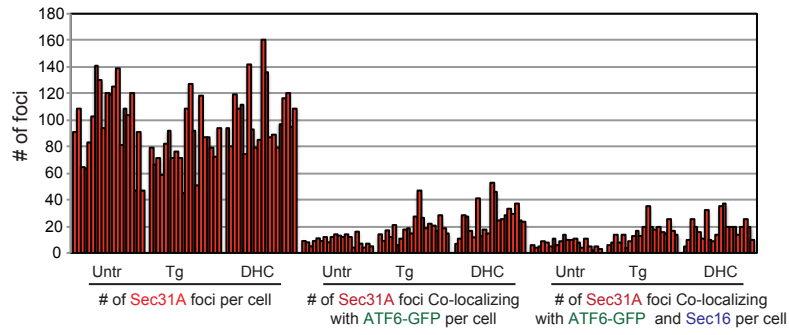
(D) Control experiments for Figure 3A are shown. In experiments described in Figure 3A, FLI-06, which inhibits COPII vesicle cargo recruitment to the ER exit site (ERES), was added to keep VSVG^{ts}-GFP in the ER. Keeping all folded VSVG^{ts}-GFP in the ER prior to treatment with DHC or DTT facilitates the clear determination of folding states, thus helping to assess the impact of DHC/DTT. Here, we show VSVG^{ts}-GFP localization without FLI-06 upon treatment with DHC or Tg. In unstressed cells, all VSVG^{ts}-GFP is folded (as revealed by a folding-specific anti-VSVG antibody (red)) and is spread throughout the secretory pathway. Treatment with DTT to disrupt ER protein folding results in unfolded VSVG^{ts}-GFP. Because DTT disrupts disulfide bonds in the ER, and thus affect folding of proteins in the ER, anti-VSVG antibody staining is reduced in the ER. In contrast, VSVG^{ts}-GFP outside of the ER still remains to be stained by anti-VSVG antibody. DHC does not affect VSVG^{ts}-GFP folding within the ER after 1 h of treatment, as is seen in unstressed cells. Since VSVG^{ts}-GFP outside of the ER should still be stained by anti-VSVG antibody, differences between DTT treated and untreated cells were less clear in comparisons to those shown in Figure 3A upon co-treatment with FLI-06.

(E) The use of a chemical chaperone, 4-phenyl Butyric Acid (4PBA,) reduced the nuclear localization of Tg-activated ATF6, but not DHC-activated ATF6. Quantification of the images are shown in Figure 3B.

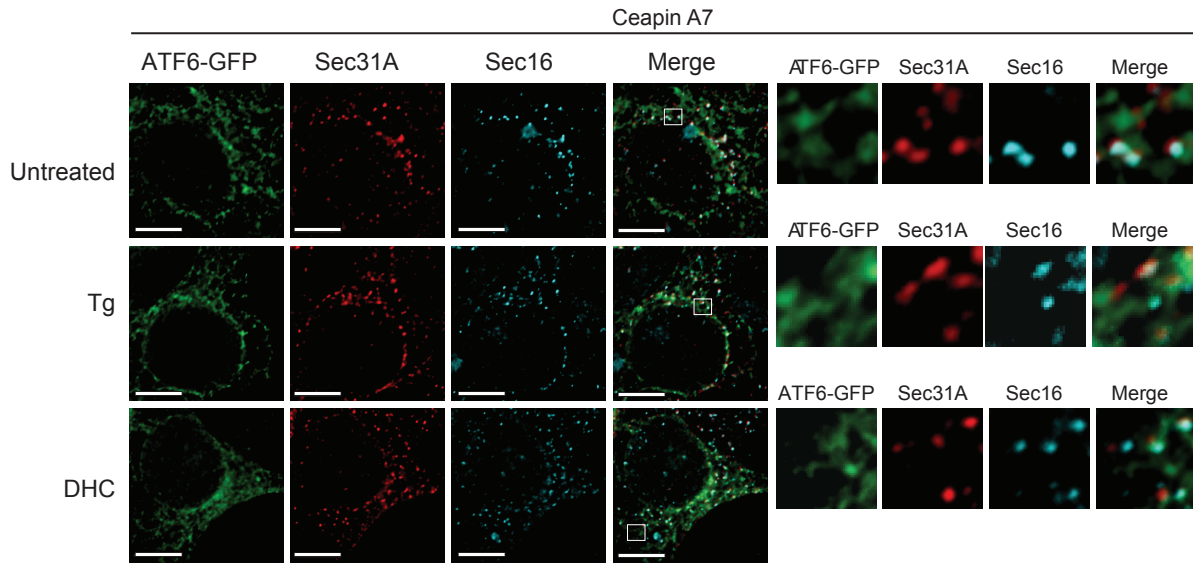
(F) HEK293 cells transfected with ATF6-GFP were left untreated or pre-treated for 60 min with 10 μ M or 20 μ M BAPTA, an intracellular Ca^{2+} chelator. Cells were then treated with 200 nM Tg or 50 μ M DHC for 60 min. Representative fields for each condition are shown. The lower panels show high magnification images of the individual cells indicated by white boxes.

(G) Quantification of ATF6-GFP activation in HEK293 cells left untreated (No BAPTA) or pre-treated (+BAPTA) for 60 min with 20 μ M BAPTA, followed by incubation with 200 nM Tg or 50 μ M DHC for 60 min shown in (F). Data represent the mean \pm SD of three independent experiments, each with at least 50 cells per sample per point. Statistical significance **p < 0.01, *p < 0.05 was calculated via unpaired two-tailed t-tests comparing untreated and treated samples.

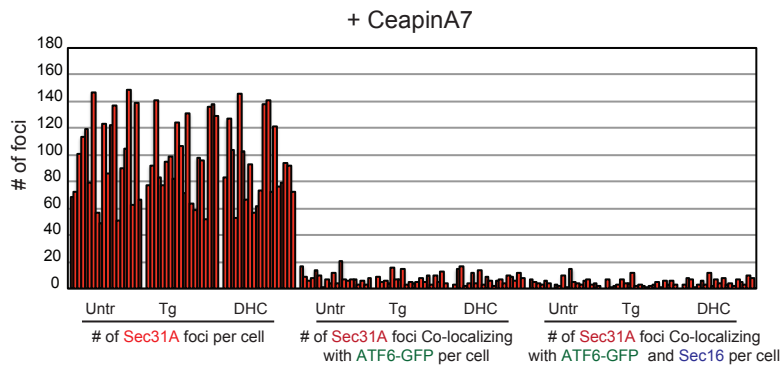
A



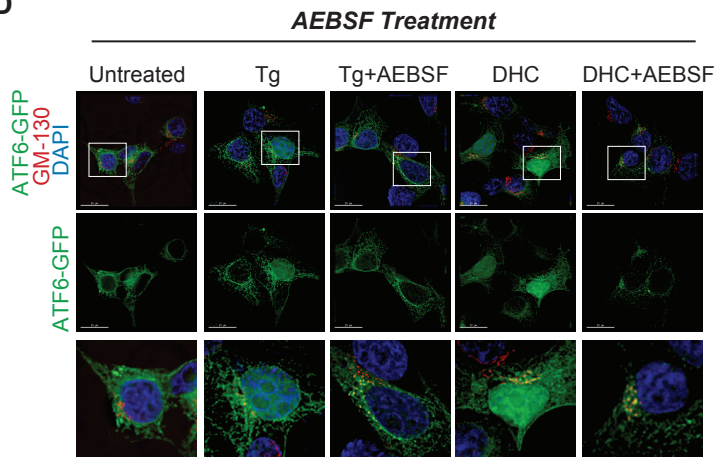
B



C



D

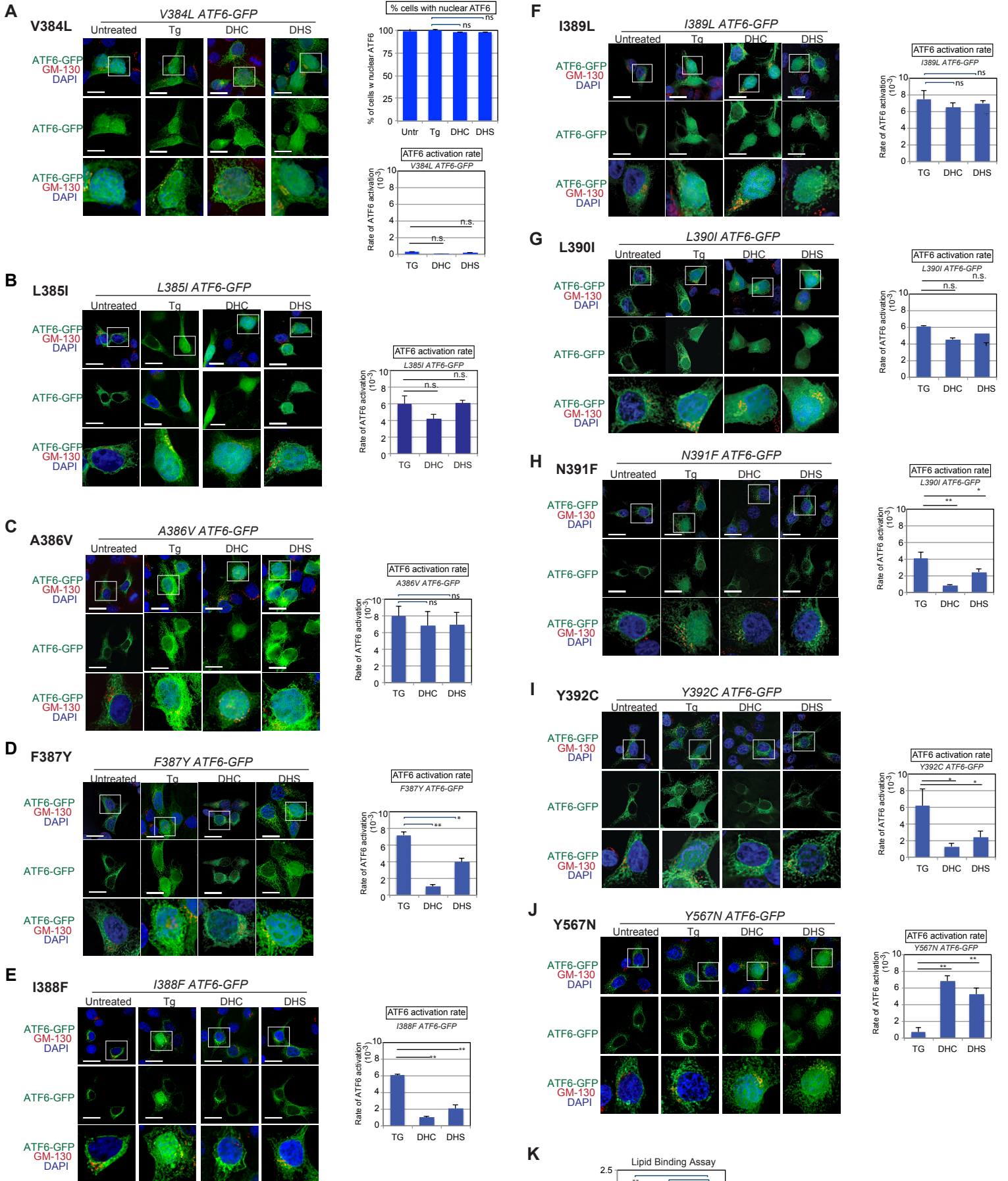


Supplemental Figure 4. Both DHC- and Tg-activated ATF6 Translocate to the Golgi via COPII Vesicles, related to Figure 4

(A) Representative primary data for the graph are shown in Figure 4B. Numbers of Sec31A-positive COPII foci (red) in untreated single cells were similar to those of Tg- or DHC-treated single cells. The number of Sec31A, a COPII vesicle associated protein that co-localized with ATF6-GFP increased with Tg and DHC treatment at similar levels, compared to those in untreated cells, suggesting that COPII vesicles with ATF6-GFP remained in the ER during Tg or DHC treatment. Similarly, co-localization of ATF6-GFP-containing COPII vesicles and the ERES (Sec16; blue) increased upon Tg and DHC treatments. Each bar represents the number of foci counted in one cell. Similar experiments were performed, at least, three independent times for quantitation shown in Figure 4B.

(B,C) Ceapin A7 blocks Tg- or DHC-induced ATF6-GFP co-localization with COPII vesicles. Images of cells with ATF6-GFP untreated, or treated with Tg or DHC in the presence of Ceapin A7, followed by staining with anti-Sec31A and anti-Sec16 antibodies are shown (B). A representative primary quantitation data for ATF6-GFP co-localized with Sec31A, a COPII vesicle component (in red), and Sec31A and Sec16, an ERES component (in blue), are quantified in each individual cell (C). Similar experiments were performed, at least, three independent times for quantitation shown in Figure 4D and E.

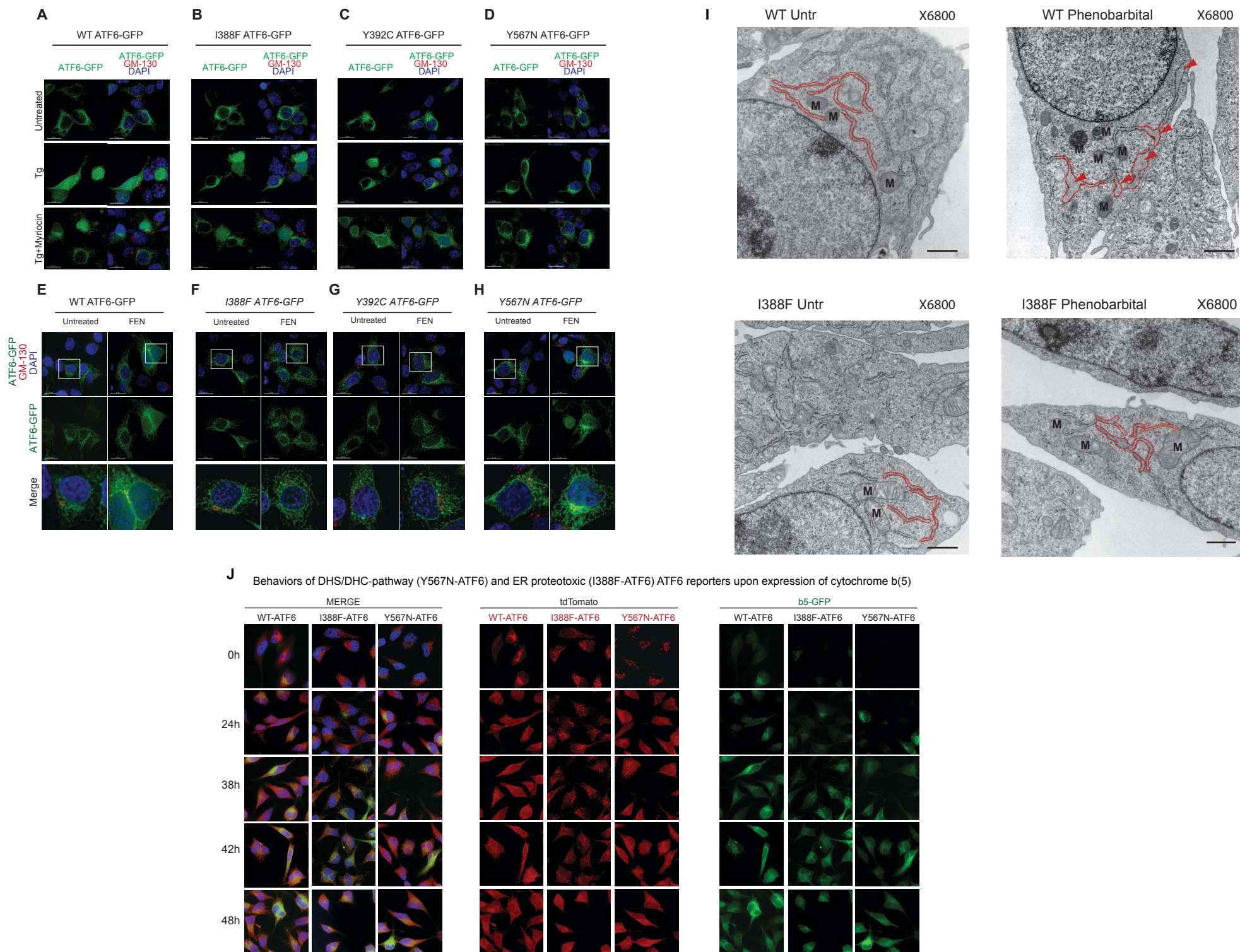
(D) Representative images showing that inactivating Golgi proteases using AEBSF, an inhibitor of the S1P and S2P proteases, blocks Tg- and DHC-induced ATF6 activation. Quantification is shown in Figure 4G.



Supplemental Figure 5. Specific Amino Acid Substitutions within the Conserved Transmembrane Motif Diminish ATF6-GFP Activation by DHC and DHS, but not by Tg, related to Figure 5.

(A–J) Representative images of ATF6-GFP containing mutations: V384L (A), L385I (B), A386V (C), F387Y (D), I388F (E), I389L (F), L390I (G), N391F (H), Y392C (I), and Y567N-ATF6 (J) treated with either Tg, DHC, or DHS, are shown. Immunostaining with anti-GM130 antibodies shows the location of the Golgi. V384L-ATF6 was constitutively activated and ATF6 was not further induced by Tg, DHC, and DHS.

(K) ^3H -DHS Binding to ATF6-GFP depends on the presence of the ATF6 sequence.



Supplemental Figure 6. I388F-ATF6 Indicates ER Proteotoxic Stress, whereas Y567N-ATF6 Indicates DHS/DHC-induced Stress in multiple experimental settings, related to Figure 6

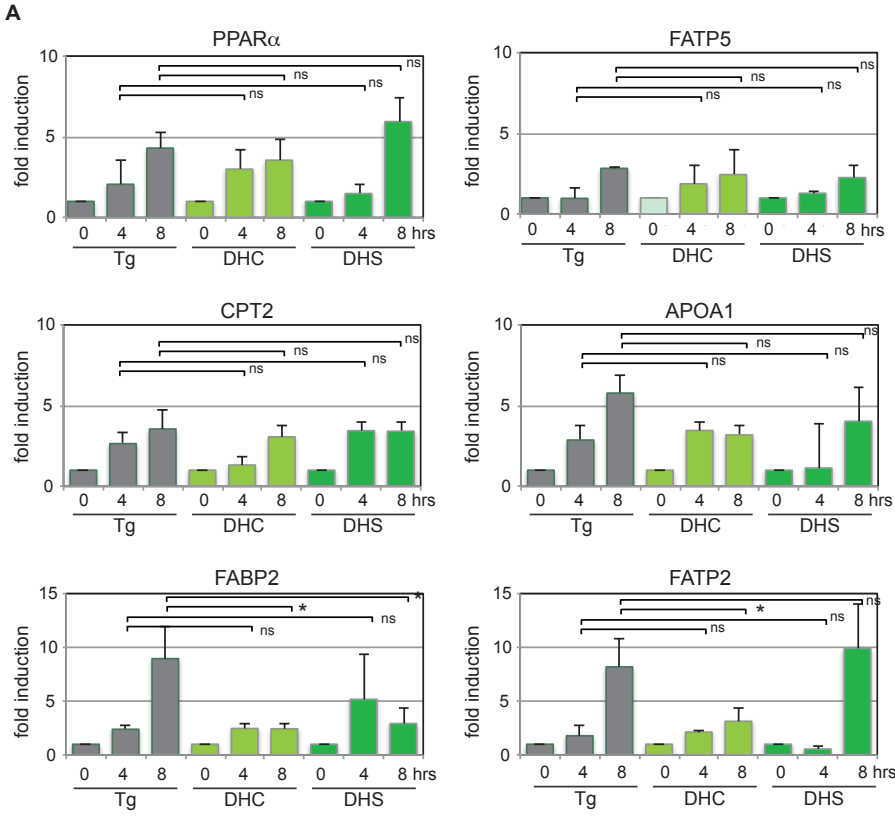
(A–D) An inhibitor of SPT, Myriocin (25 mM), reduced WT-ATF6 activation (A), but not activation of I388F-ATF6 (B), Y392C-ATF6 (C), and Y567N-ATF6 (D).

(E–H) Representative field images of HEK293 cells expressing WT (E), I388F- (F), Y392C- (G), or Y567N-ATF6 (H) that were treated with Fenretinide (FEN). ATF6-GFP activation rate is calculated in Figure 6B. Data represent the mean \pm SD of three independent experiments, each with at least 50 cells per sample per point. Statistical significance ** $p < 0.01$, * $p < 0.05$ was calculated via unpaired two-tailed t-tests comparing untreated and treated samples.

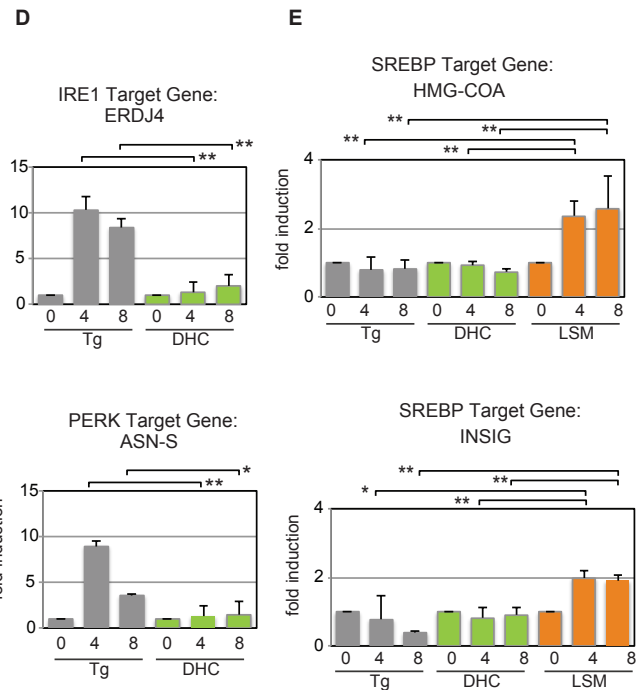
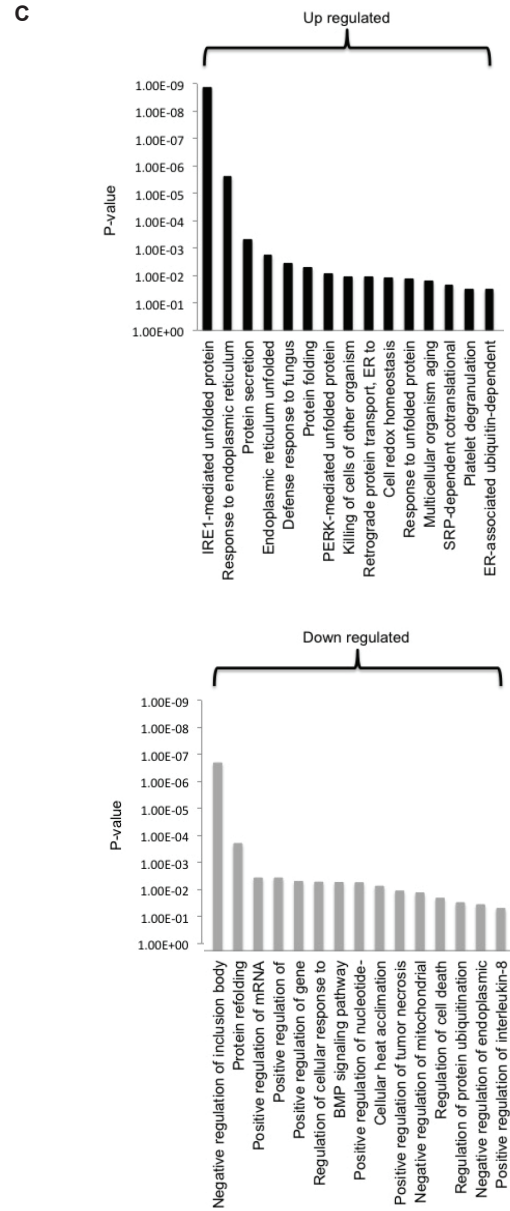
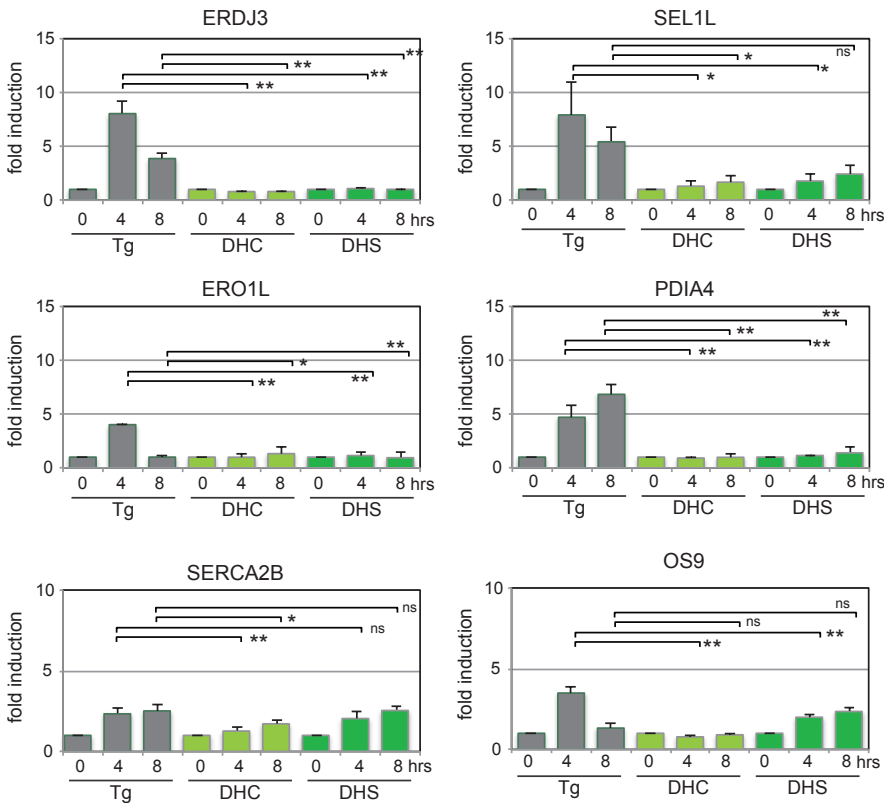
(I) Additional EM images of *atf6*^{-/-} MEFs expressing WT ATF6 or I388F-ATF6 that were treated with phenobarbital (PB). Parts of the ER membrane are traced with red lines and red arrowheads show dilated ER, which is not seen at significant levels in I388F-ATF6 cells. M: mitochondria.

(J) HeLa cells with inducible b(5)-GFP in a Dox-inducible cell line system were transfected with WT ATF6 tdTomato, I388F ATF6 tdTomato, or Y567N tdTomato for 24 hrs and Dox was removed to start b5-GFP expression for indicated length of time up to 48hrs. Expression of b(5) has previously been shown to expand the ER (Maiuolo et al., 2011). WT-ATF6 tdTomato, I388F-ATF6 tdTomato, or Y567N-ATF6 tdTomato was imaged in the red channel while b(5) expression visualized by the GFP signal was imaged in the green channel. Representative fields are shown. I388F-ATF6 cells responds to mre slowly to increase b(5) expression in the ER.

ATF6 target lipid function genes



ATF6 target ER chaperone and protein folding components genes



Supplemental Figure 7. DHS/DHC Preferentially Activates Transcription of ATF6 Target Lipid Biogenesis Genes, related to Figure 7.

(A) Transcriptional induction of ATF6-specific lipid function genes was induced by DHS/DHC. ER lipid genes (namely PPAR α : peroxisome proliferator activated receptor alpha, FATP5: fatty-acid transport protein 5, CPT2: carnitine palmitoyltransferase 2, APOA1: apolipoprotein A1, FABP2: fatty acid binding protein 2, FATP2: fatty-acid transporter protein 2 (Yamamoto et al., 2010)) are shown.

(B) Transcriptional induction of ATF6-specific ER chaperone genes was induced by Tg, but much less induced by DHS/DHC. ER chaperones and other ER luminal components (namely ERDJ3: DnaJ heat shock protein family (Hsp40) member B11, SEL1L: SEL1L ERAD E3 ligase adaptor subunit, ERO1L: endoplasmic reticulum oxidoreductase 1, PDIA4: protein disulfide isomerase family A member 4, SERCA2B: ATPase sarcoplasmic/endoplasmic reticulum Ca²⁺ transporting 2, OS9: OS9, endoplasmic reticulum lectin (Shoulders et al., 2013, Wu et al., 2013) are shown.

(C) Clusters of GO terms genes that were transcriptionally upregulated with Tg treatment (shown as Upregulated), but not so much with DHC. Conversely, those that were down regulated with DHC (shown as Down regulated) but not with Tg are shown. *P*-values are shown.

(D) Transcription of the IRE1-XBP1 target gene, *ERdj4*, (Shoulders et al., 2013), and the PERK-ATF4 target gene, *Ans-S* (Gjymishka et al., 2009) are not induced by DHC.

(E) Transcription of SREBP target genes, HMG-CoA reductase (HMG-CoA) and Insig, is not induced by DHC treatment (light green) or by Tg treatment (grey), whereas low serum medium (LSM), a known SREBP transcription activating condition (orange), activates their transcription.

	<i>Forward Primer (5' - 3')</i>	<i>Reverse Primer (5' - 3')</i>	<i>Gene ID:</i>	<i>Gene Name:</i>	<i>Gene Description:</i>
LRP1	GAGCTGAACCCACGCTTTG	GGTAGACTGCGCACTCCGATAC	4035	LRP1	LDL receptor related protein1
ACOX1	GAGCTGCTCACAGTACTCG	CACGATCATCTTCCCATCCT	51	ACOX1	acyl-CoA oxidase 1
PPARA	GCACCATTGCCATTTCGATACA	GCACCATTGCCATTTCGATACA	5465	PPARA	peroxisome proliferator activated receptor alpha
FATP5	TCGGATCTGGGAATTCTACG	AAGCTCAAAGGGAGTCAGCA	10998	SLC27A5	solute carrier family 27 member 5
CPT2	GGGAAGGGAAGGAGACGAG	CCAAGACTGCGTCAGGAC	1376	CPT2	carntine palmitoyltransferase 2
APOA1	GTGGCTCTGGTCTTCTGAC	ACGGTTGAACCCAGAGTGTG	335	APOA1	apolipoprotein A1
FABP2	CCAGGAGAACTTTCAGCCATTG	TGTCCTTCCCTTTCGGATGA	2169	FABP2	fatty acid binding protein 2
FATP2	CAACACACCGCAGAAACCA	ATTTCCAGGGCTTTTTTCA	11001	SLC27A2	solute carrier family 27 member 2
APOB	TGTGGCAAAGGAAACAATGA	AATCCTGCAGATTGGAGTGG	338	APOB	apolipoprotein B
MVD	AAGCAGACGGGCAGTACAGT	CCTGGAGGTGTCATTGAGGT	4597	MVD	mevalonate diphosphate decarboxylase
BIP	GCCTGTATTTCTAGACCTGCC	TTCATCTTGCCAGCCAGTTG	3309	HSPA5	heat shock protein family A (Hsp70) member 5
HERPUD	AACGGCATGTTTTGCATCTG	GGGGAAGAAAGTTCCGAAG	64224	HERPUD2	HERPUD family member 2
ERDJ3	TGGAAGAAGTGTACGCAGGA	GACAGTTGCATTTCCGTTTG	51726	DNAJB11	DnaJ heat shock protein family (Hsp40) member B11
SEL1L	ATCTCCAAAAGGCAGCAAGC	TGGGAGAGCCTTCCCTCAGTC	6400	SEL1L	SEL1L ERAD E3 ligase adaptor subunit
ERO1L	AAGGGCTCTCTCAAAGTGCT	AGCTGAAAATCTGGACGCTCA	30001	ERO1A	endoplasmic reticulum oxidoreductase 1 alpha
PID4	AGTGGGAGGATGTCAATGC	TGGCTGGGATTTGATGACTG	9601	PID4	protein disulfide isomerase family A member 4
SERCA2B	TTAAAGCAACTGTCTATTTCTGCTG	AGTCAGAAAAAGCAAAACAAAATCTA	488	ATP2A2	ATPase sarcoplasmic/endoplasmic reticulum Ca2+ transporting 2
CALR	ACATCAGGAGCTAAAAGCAGCC	TGAAACATACGTACCCGCA	811	CALR	calreticulin
GRP94	GGGAGGTCACCTTCAAGTCG	CTCGAGGTGCAGATGTGGG	7184	HSP90B1	heat shock protein 90 beta family member 1
OS9	GCTGGCTGACTGATGAGGAT	CGGTAGTTGCTCCAGCTC	10956	OS9	OS9, endoplasmic reticulum lectin
ERDJ4	GGGAGGAGGCGCTAGGTC	ATCCTGCACCCTCCGACTAC	4189	DNAJB9	DnaJ heat shock protein family (Hsp40) member B9
ASNS	GTTGAACATCAGTTGATGATG	CCTGGGTAATGGCGTTC	440	ASNS	asparagine synthetase (glutamine-hydrolyzing)
HMG-COA	CAGGATGCAGCACAGAATGT	CTTTGCATGCTCCTTGAACA	3156	HMGCR	3-hydroxy-3-methylglutaryl-CoA reductase
INSIG	TGCAGATCCAGCGGAATGT	CCAGGCGGAGGAGAAGATG	3638	INSIG2	insulin induced gene 1

***Supplemental Table 1.* PCR Primers Used for ATF6 Target Gene, related to Figure 7**